Figure 2. *Visualization of the instantaneous local excitation vectors (small arrows on the heart models), depolarization vector (large arrows on the torso models), and the corresponding ECG (left) for the estimation of excitation sequence. Data for patient #1 at different times from the onset of the QRS complex are shown as time-lapse images. For clarity, only a single lead of the ECG (II lead) is shown and the arrangement of each panel differs from the original computer display.*

Computation

All the program code was written in FOR-TRAN in our laboratory. Simulations were performed using an SGI Rackable C2108-TY10 server (Intel Xeon X5690 [3.46 GHz], Intel, Santa Clara, CA, USA). With the total number of degrees of freedom set to three hundred million, it took 6 hours to compute a single cardiac cycle. The numerical data was visualized using commercial software (MicroAVS: Advanced Visual Systems, Waltham, MA, USA, and Avizo: VSG, Burlington, MA, USA).

Results

Heart models with and without non-excitable regions for all the patients are shown together with the corresponding torso models in Figure 3. In the hearts of patients #2 and #3, the regions of nonexcitable tissue are indicated below. The size and shape of the heart and torso varied considerably among the patients. The results of the simulations are described separately for each patient.

Patient #1

Since no organ abnormalities were reported for this patient, only the sequence of excitation propagation was adjusted. As for the optimization of the distribution of cell types, no adjustment was made in this case. With these settings, the activation and repolarization sequences of the heart (Fig. 4A) and the resulting changes in the body surface potential (Fig. 4B) were computed fairly rapidly (see also the supplementary movie S2). The simulated ECG with narrow QRS complexes and positive T waves in most of the leads corresponds well with the actual one (Fig. 4C).

Patient #2

According to the information from the scintigram, infarcted regions were set (Fig. 3 center
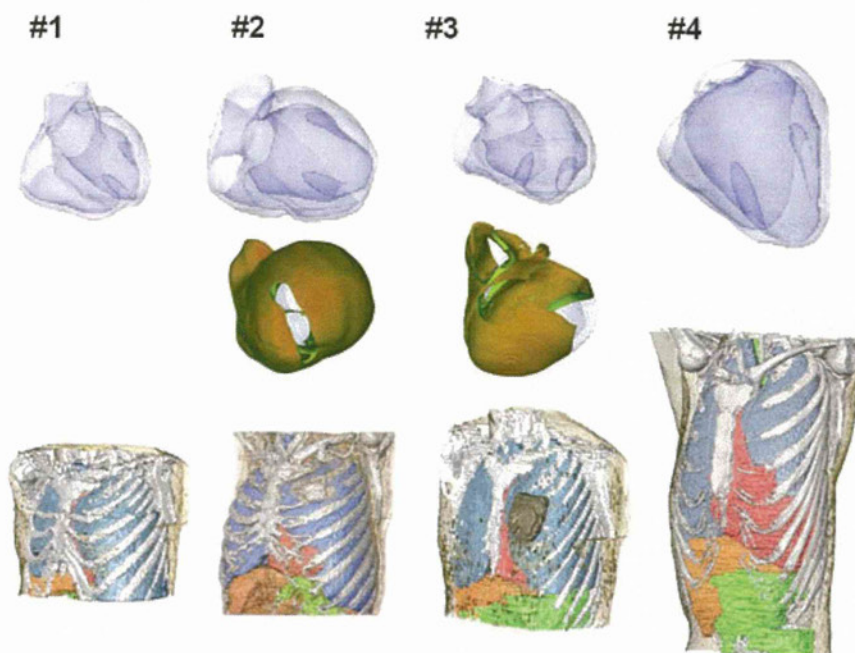
Figure 3. *Finite element models of the heart and torso for the patients studied. For patients #2 and #3, non-excitable regions are shown under the heart models. Scales are different for the heart and torso models, but the same for all patients for ease of comparison.*
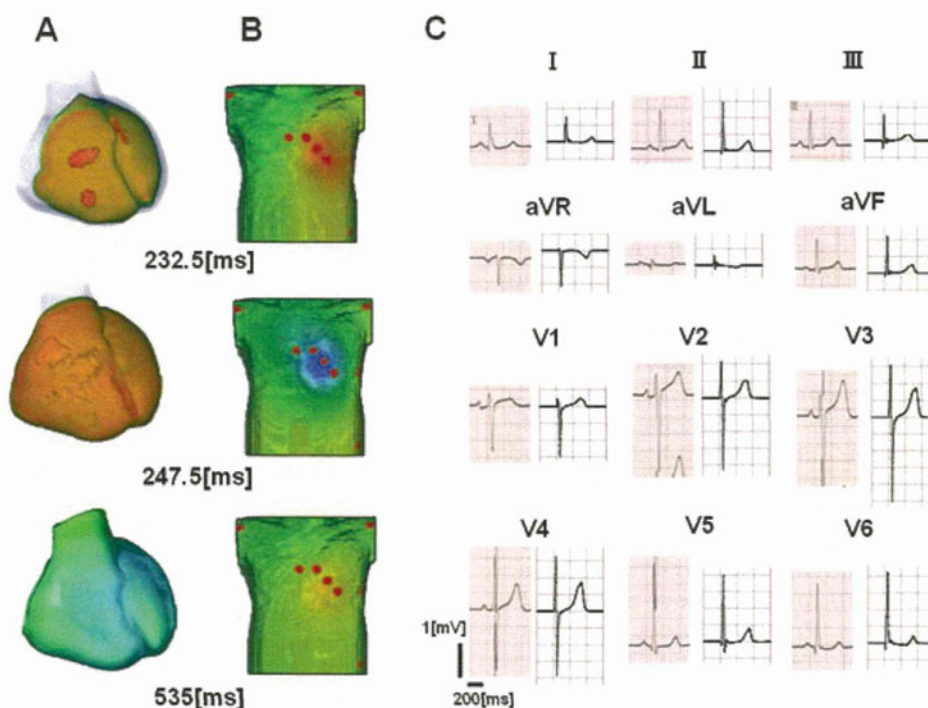

Figure 4. *Propagation of excitation and repolarization (A), body surface potential map (B) as time lapse images, and ECG for patient #1 under control conditions. In (C), the simulated ECG is shown on the right and the actual ECG on the left for each lead. The red dots on the torso (B) represent the ECG leads.*

Figure 5. *Propagation of excitation and repolarization (A), body surface potential map (B) as time lapse images, and ECG for patient #2 under control conditions. In (C), the simulated ECG is shown on the right and the actual ECG on the left for each lead. The red dots on the torso (B) represent the ECG leads.*
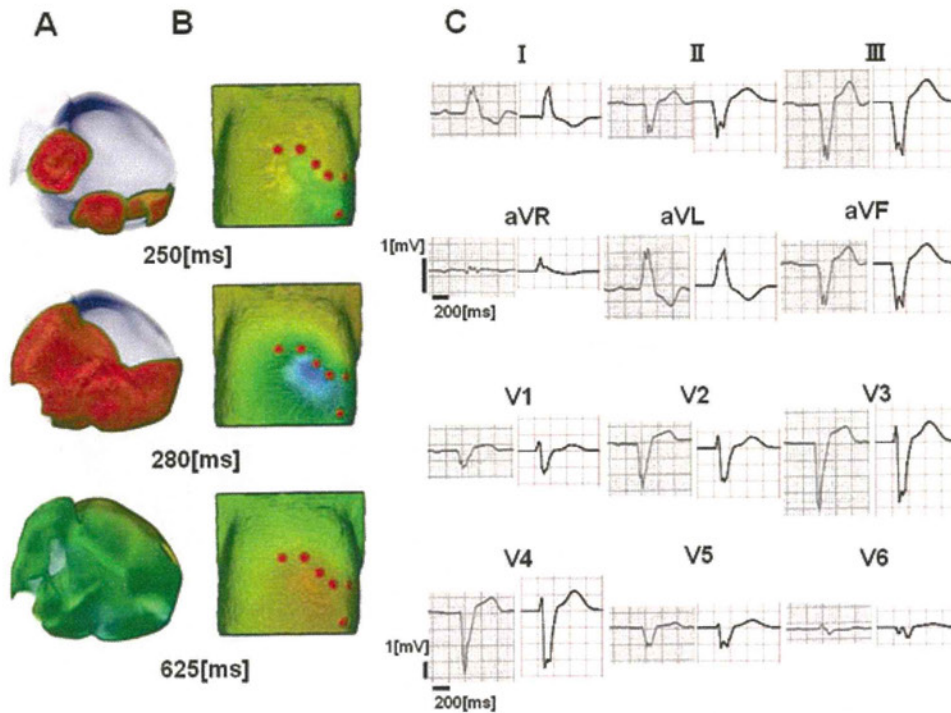
panel). Based on the clinical diagnosis of a complete left bundle branch block (CLBBB), the earliest excitation sites were eliminated from the left ventricular endocardium and the failing myocyte model was applied to the entire ventricle. Time-lapse images of the membrane potential and body surface potential are shown in Figure 5A and B (see also the supplementary movie S3), while a comparison of the ECGs is presented in Figure 5C. Again, reasonable agreement is observed. Based on the history of the patient's current illness, a CRT device was implanted. We placed the pacing leads at the site of actual implantation determined from the CT images to simulate the CRT. Although a simultaneous bi-ventricular pacing protocol (no inter-ventricular delay) was programmed for this patient, we needed to advance the right ventricular (RV) stimulation by 70 ms to achieve reasonable agreement in the ECGs. In our opinion, this delay can be accounted for by the electrical latency during left ventricular (LV) stimulation from the coronary veins[17] and in fact, a comparison of the ECGs for RV and LV pacing alone supports this idea (Fig. 6C inset). The mode of excitation under CRT is shown in Figure 6A and B (see also the supplementary movie S4), with a comparison

of ECGs presented in Figure 6C. Because we did not modify the morphology of the heart and its tissue characteristics determined for the baseline ECG, that is, as shown in Figure 5, the good correspondence after the CRT serves as an independent test for the validity of the model.

Patient #3

In this patient with a dilated phase of hypertrophic cardiomyopathy, an extended and irregular area of perfusion defect is observed in the scintigram. The ECG shows an extremely complex pattern of excitation that differs from the typical CLBBB pattern (Fig. 7C), and this led to a long series of iterative adjustments of both the defect region and earliest excitation sites. In the beginning, the failing myocyte model was allocated to the entire ventricle but, to reproduce the upright T waves in the right precordial leads (V1-V3), we introduced the endocardial, M-, and epicardial cell models transmurally. Final results of the activation sequences and a comparison of the ECGs are shown in Figure 7 (and also in the supplementary movie S5). Although disagreements are seen in some segments, the overall pattern of the complex ECG is well
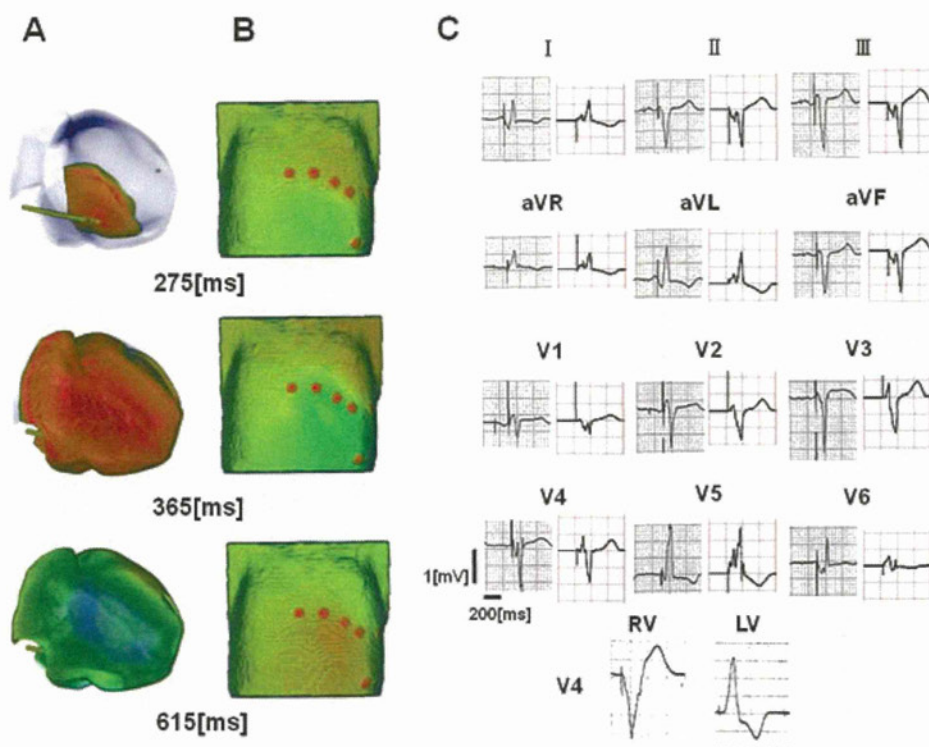
Figure 6. *Propagation of excitation and repolarization (A), body surface potential map (B) as time lapse images, and ECG for patient #2 under bi-ventricular pacing. In (C), the simulated ECG is shown on the right and the actual ECG on the left for each lead. The red dots on the torso (B) represent the ECG leads, and the stick in the heart chamber (A) represents the right ventricular pacing lead. Inset: V4 leads for this patient under RV and LV pacing. A significant delay between the stimulus spike and QRS wave is observed for LV pacing.*

reproduced. The ECG after the CRT was also simulated for this patient according to clinical records, and, as illustrated in Figure 8 (and also in the supplementary movie S6), it shows reasonable agreement with the actual one. Because no further adjustment was made to the baseline model in this case either, the good agreement can be taken to indicate that the modeling may not be unique, but is at least a close solution to this inverse problem.

Patient #4

The heart of this patient was severely dilated because of aortic regurgitation. Duration of the QRS complex was elongated (>140 ms), but the presence of a Q wave in the V6 lead excluded the diagnosis of CLBBB (Fig. 9C). Accordingly, we considered that the widening of the QRS was caused simply by the enlargement of the heart and we started making adjustments from the normal activation sequence, similar to the procedure for patient #1. However, because the duration of the QRS complex was not comparable with the actual data, we reduced the conduction

velocity by 68% in the fiber direction and 25% in the cross fiber direction. The final data for excitation propagation, body surface potential, and the ECG are shown in Figure 9, together with the actual ECG for comparison. Once again a reasonable match was achieved (see also the supplementary movie S7). However, under pacing conditions, there is a slight disagreement in the QRS morphology in leads I and VL (Fig. 10) (see also the supplementary movie S8). Such disagreements could be corrected by adjusting the property of the heart model determined under control conditions. Nevertheless, this was not done, owing to a lack of clinical data to rationalize it.

Cross-Correlation

Figure 11 shows an example of the relation between the cross-correlation and the matching of ECG wave form with the corresponding excitation propagation sequence. Each vector in each panel corresponds to the ECG amplitude in the specific lead with the same angle as that in the inset
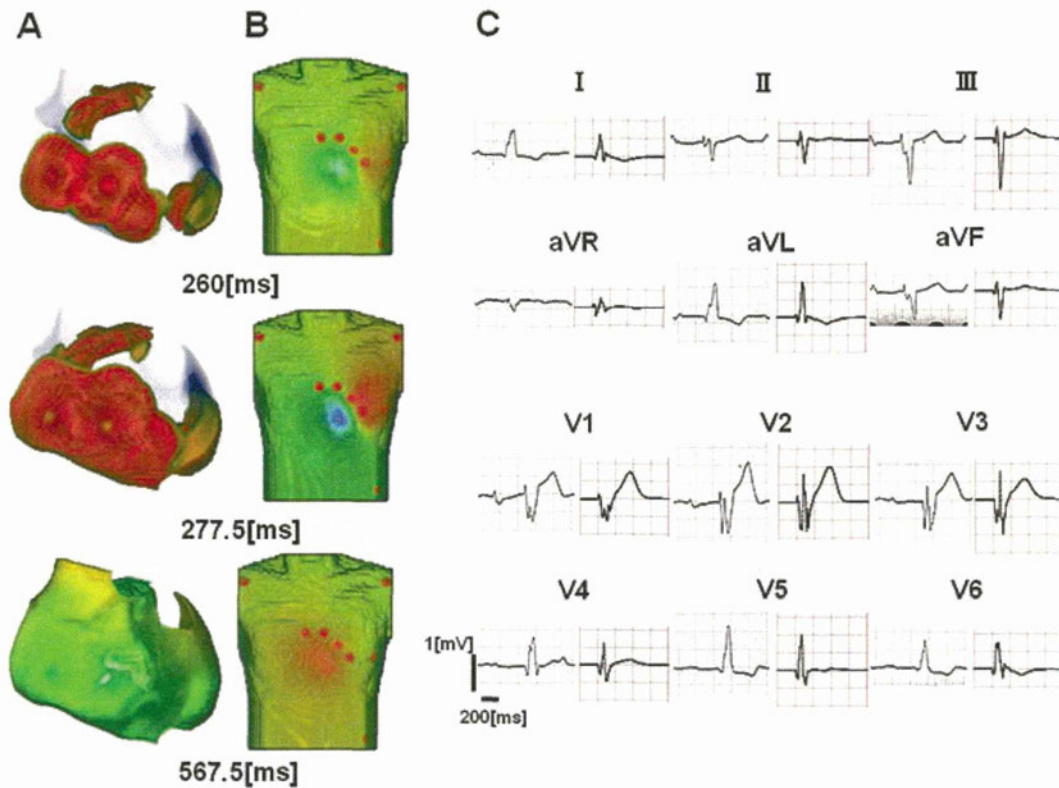
Figure 7. *Propagation of excitation and repolarization (A), body surface potential map (B) as time-lapse images, and ECG for patient #3 under control conditions. In (C), the simulated ECG is shown on the right and the actual ECG on the left for each lead. The red dots on the torso (B) represent the ECG leads.*

at a certain time. Therefore, the similarity of the vector clusters indicates a correct fit of the ECG waveform. Compared with the actual ECG data (top row), the vector cluster in simulation A (middle row) differs significantly at all time points, yielding a cross-correlation value of 0.615. A shift in the earliest excitation sites in simulation B (bottom row) reproduced large upward vectors observed in the actual ECG and increased the cross-correlation to 0.896. For visibility only the precordial vectors are shown; however, limb lead vectors were also taken into consideration. Table II summarizes the cross-correlation of the simulated ECGs for all cases studied (Figs. 4 to 10). Fairly good correlations (>0.65) were obtained for both the baseline and pacing conditions, except for that under pacing in case 2.

Discussion

With the advent of high performance computers, realistic simulation of cardiac electrophysiology, in which cell models of electrophysiology are implemented in the image based finite element models of the heart, is now possible. However, a limited number of attempts have been made

with respect to patient-specific ECG simulations coupled with image-based torso models. In this study, although our preliminary approach yielded promising results, we also identified problems to be overcome in future studies.

Patient-Specific ECG Simulation

An alternative approach to the realization of patient specific ECG simulation is, of course, solving the inverse problem, which researchers have pursued for several years.[3,5,18–20] Hitherto, attempts have been successful only in the estimation of epicardial maps,[3] owing to the well-known ill-posed nature of the problem. However, the forward problem approach adopted in this study can provide information on the activation and repolarization sequences within the wall, but this requires iterative simulations with manual adjustment of the parameters. To reduce the computation time required for such repeated ECG simulations, various solution techniques have been proposed, including the BEM[7] and finite element method based on the two step approach.[9] In this study, we used our previously proposed parallel multi-grid method[11] to solve the dynamic
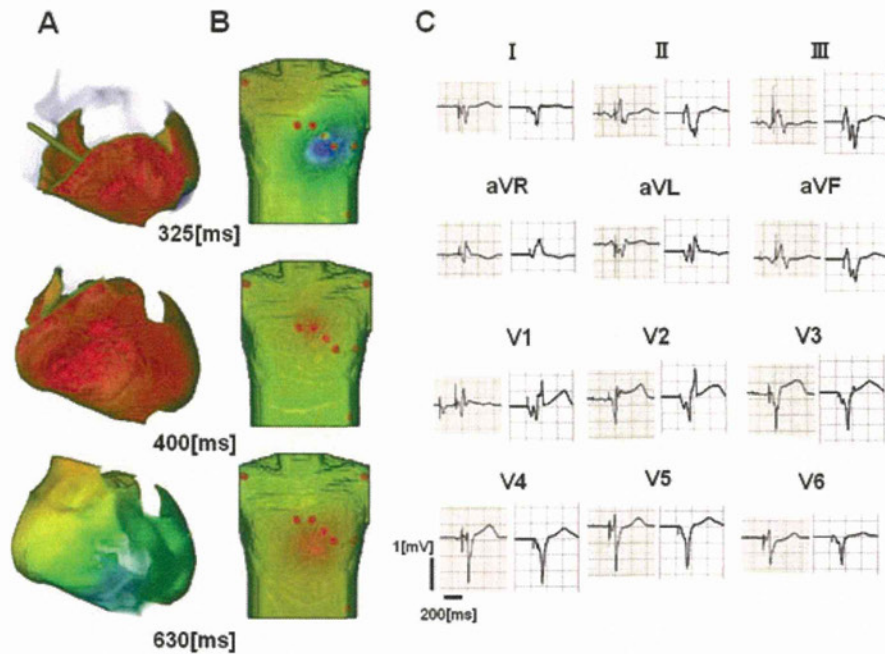
Figure 8. *Propagation of excitation and repolarization (A), body surface potential map (B) as time lapse images, and ECG for patient #3 under bi-ventricular pacing. In (C), the simulated ECG is shown on the right and the actual ECG on the left for each lead. The red dots on the torso (B) represent the ECG leads, while the stick in the heart chamber (A) represents the right ventricular pacing lead.*
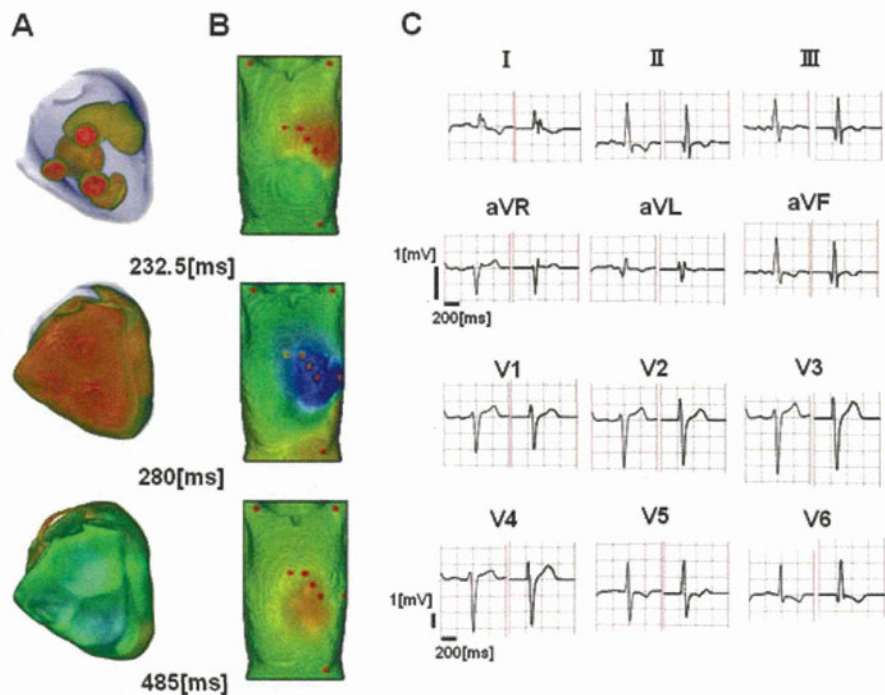
Figure 9. *Propagation of excitation and repolarization (A), body surface potential map (B) as time lapse images, and ECG for patient #4 under control conditions. In (C), the simulated ECG is shown on the right and the actual ECG on the left for each lead. The red dots on the torso (B) represent the ECG leads.*

Figure 10. *Propagation of excitation and repolarization (A), body surface potential map (B) in time lapse images, and ECG for patient #4 under bi-ventricular pacing. In (C), the simulated ECG is shown on the right and the actual ECG on the left for each lead. The red dots on the torso (B) represent the ECG leads while the stick in the heart chamber (A) represents the right ventricular pacing lead.*
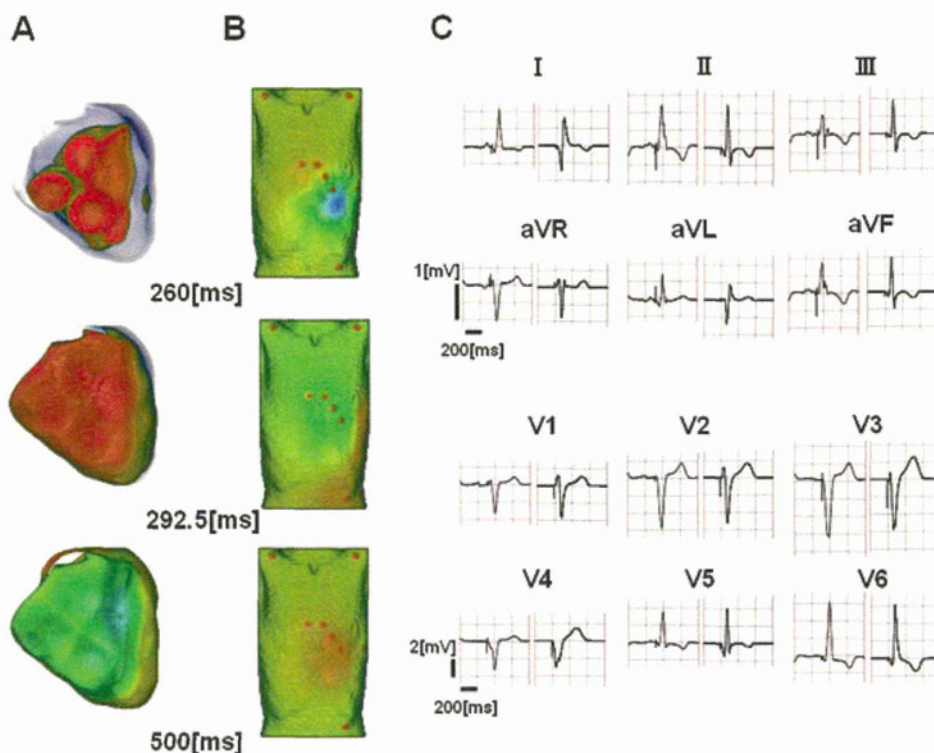
bi-domain problem within a practical time interval (∼80 min). One of the advantages of this approach is its ability to evaluate the influence of surrounding tissue on the electrical activity of the heart, although this influence was not evaluated in this study. We also developed an interactive system for the simultaneous visualization of 3D wave fronts and the vector ECG to accelerate the adjustment of the excitation sequences to reproduce the QRS wave morphology. Even with such developments, however, the total time required to model the complex ECG for patient #2 was quite long. A hybrid approach using both the inverse and forward problems may help in providing a more efficient solution.

Goodness of Fit

To quantify the goodness of fit, we calculated the cross-correlation between the simulated and actual ECGs to obtain reasonable values. However, such neutral numerical indices may not correlate with the visual impression and in fact, clinical diagnosis relies on the characteristic morphology

of each segment of the ECG. Furthermore, we cannot be sure whether the morphological fit ensures validity of the parameters set in the model in the absence of clinical measures for direct comparison. However, reproducibility of the model can be evaluated by referring to other clinical data. In this sense, our simulation of the ECG after the CRT implantation (Figs. 6, 8, and 10, and Table II) provides strong support for the validity of our modeling.

Limitations

Although the number of cases in this study was small, the diversity in pathology could suggest potential applicability of this technique to a wide range of diseased hearts. However, cases in which mutant ion channels are expected to have a complex effect on the electrophysiology were not included, and this is left for future study.

The current simulation based on the available clinical data includes many uncertainties in the modeling of both the heart and the torso. Fiber orientation is known to have a significant
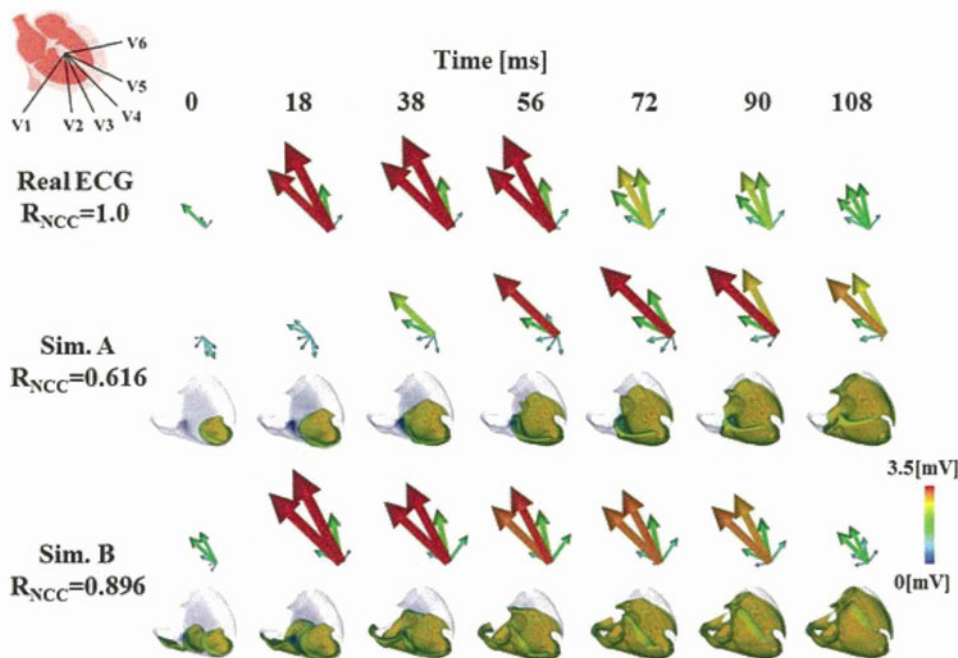
Figure 11. *Sequential changes in ECG vector and ventricular excitation. In each panel, each vector represents the amplitude of the specific precordial lead as indicated in the inset. Top row: actual ECG, and middle and bottom rows: simulation results with poor (Sim. A $R_{NCC} = 0.615$) and good (Sim. B $R_{NCC} = 0.896$) cross-correlations, respectively, for case #2. For the simulation results, the accompanying ventricular excitation of the models is shown. The numbers at the top indicate the time since the onset of the QRS complex.*

influence on the conductivity and mechanics of the myocardial tissue.[21–23] Since there is no measure for recording the fiber orientation in a beating heart, we had to adopt the only published data for both normal and diseased hearts. The use of the scintigram absolutely limited the segmentation of myocardial tissue in terms of space and character. We intend to use magnetic resonance imaging (MRI) data with enhancements for the modeling, but even with this information, fine-tuning of the cell model to reproduce reality will be difficult. As an approximation, we used a single parameter set for both the normal and failing myocyte models.[12,16,24]

Uncertainties were also identified in the torso. Dössel's group reported that fat is important

in the morphology of the ECG, yet its conductivity varies considerably in the literature.[9,25] However, we also noted that such variation in conductivity scales the waveform, while retaining the overall characteristics. Accordingly, we adjusted the conductivity of the subcutaneous fat tissue to adjust the amplitudes of the ECG; however, further refinement of the model for each patient based on conductivity metric is needed. The influences of variation in myocardial conduction velocity and slowing or blockage in the His-Purkinje system are also important issues that need to be addressed in future studies incorporating cutting edge experimental results.

Furthermore, in this study, we simulated only the electrical activity with a static heart model; however, the feedback influence of mechanical activity on the electrical activity of the heart is well established and simulations taking into account such effects have been reported.[26–29]

Finally, although the calculation of the cross-correlation coefficient shows that the presented results are the best from the models tested, they do not ensure optimality of the model. This is because of the inclusion of the manual iteration part in the

Table II.

Cross-correlation

Case	1	2	3	4
Baseline	0.748	0.896	0.645	0.795
Pacing		0.653	0.579	0.842

procedure, which should be automated in future studies.

Future Directions

To extend the applicability of ECG simulation to a wider range of diseases at various stages, modeling of the atria, coronary circulation, and other anatomical structures coupled with the integration of multiphysics phenomena is necessary. However, such detailed modeling necessitates the development of diagnostic techniques enabling in vivo recording of the micro-anatomical structure, tissue properties, and metabolism. Detailed simulations also require acceleration of the modeling process at each stage. Parametric modeling is a powerful approach,[30] but the final fine-tuning still remains for personalized models. Further studies and developments are clearly needed.

Despite its long history, the inverse problem approach still cannot provide a unique solution for the determination of multiple activation sites or the sequence of transmural activation even

when utilizing the body surface mapping data. Alternatively, we adopted the forward problem approach in this study to obtain 3D pattern excitation and repolarization sequences, which reproduces an ECG with reasonable agreement. The number of trials may not be large enough to ensure convergence, but, acceleration of the simulation using a high performance computer will allow us to perform a true exhaustive search to determine the best-fit result in the near future.

Conclusions

We have created patient specific models of the heart and torso for patient-specific simulation of the body surface ECG based on clinical data to successfully reproduce the patient's characteristics. The good agreement obtained for the ECGs under bi-ventricular pacing provides strong support for the validity of the models. The current simulation results not only help us to understand the cellular basis of the ECG, but also open the possibility of an integrative heart simulator for clinical applications.

References

1. Lee J, Niederer S, Nordsletten D, Le Grice I, Smaill B, Kay D, Smith N. Coupling contraction, excitation, ventricular and coronary blood flow across scale and physics in the heart. Phil Trans R Soc A 2009; 367:2311–2331.
2. Trayanova NA. Whole-heart modeling applications to cardiac electrophysiology and electromechanics. Circ Res 2011; 108:113–128.
3. Ramanathan C, Ghanem RN, Jia P, Ryu K, Rudy Y. Noninvasive electrocardiographic imaging for cardiac electrophysiology and arrhythmia. Nature Medicine 2004; 10:422–428.
4. Potse M, Dubé B, Richer J, Vinet A, Gulrajani RM. IEEE Trans Biomed Eng 2006; 53:2425–2435.
5. Farina D, Jiang Y, Dössel O. Acceleration of FEM-based transfer matrix computation for forward and inverse problems of electrocardiography. Med Biol Eng Comput 2009; 47:1229–1236.
6. Vigmond E, Vadakkumpadan F, Gurev V, Arevalo H, Deo M, Plank G, Trayanova N. Towards predictive modelling of the electrophysiology of the heart. Exp Physiol 2009; 94:563–577.
7. Fischer G, Tilg B, Modre R, Huiskamp GJM, Fetzer J, Rucker W, Wach P. A bidomain model based BEM-FEM coupling formulation for anisotropic cardiac tissue. Ann Biomed Eng 2000; 28:1229–1243.
8. Xue J, Gao W, Chen Y, Han X. Study of repolarization heterogeneity and electrocardiographic morphology with a modeling approach. J Electrocardiol 2008; 41:581–587.
9. Keller DUJ, Weber FM, Seemann G, Dossel O. Ranking the influence of Tissut conductivities on forward-calculated ECGs. IEEE Trans Biomed Eng 2010; 57:1568–1576.
10. Okada J, Washio T, Maehara A, Momomura S, Sugiura S, Hisada T. Transmural and apicobasal gradients in repolarization contribute to T-wave genesis in human surface ECG. Am J Physiol 2011; 301:H200–H208.
11. Washio T, Okada J, Hisada T. A parallel multilevel technique for solving the bidomain equation on a human heart with Purkinje fibers and a torso model. SIAM Review 2010; 52:717–743.
12. Ten Tusscher KHWJ, Noble D, Noble PJ, Panfilov AV. A model for human ventricular tissue. Am J Physiol 2004; 286:H1573–H1589.
13. Ten Tusscher KHWJ, Hren R, Panfilov AV. Organization of ventricular fibrillation in the human heart. Circ Res 2007; 100:e87–e101.
14. Durrer D, van Dam RT, Freud GE, Janse MJ, Meijler FL, Arzbaecher RC. Total excitation of the isolated human heart. Circulation 1970; 41:899–912.
15. Glukhov AV, Fedorov VV, Lou Q, Ravikumar VK, Kalish PW, Schuessler RB, Moazami N, et al. Transmural dispersion of repolarization in failing and nonfailing human ventricle. Circ Res 2010; 106:981–991.
16. Winslow RL, Greenstein JL, Tomaselli GF, O'Rouke B. Computational models of the failing myocyte: Relating altered gene expression to cellular function. Phil Trans R Soc A 2001; 359:1187–1200.
17. Herweg B, Ilercil A, Madramootoo C, Krishnan S, Rinde-Hoffman D, Weston M, Curtis AB, et al. Latency during left ventricular pacing from the lateral cardiac veins: A cause of ineffectual biventricular pacing. Pacing Clin Electrophysiol 2006; 29:574–581.
18. Barber MR, Fischmann EJ. Heart dipole regions and the measurement of dipole moment. Nature 1961; 192:141–142.
19. Modre R, Tilg B, Fischer G, Wach P. Noninvasive myocardial activation time imaging: A novel inverse algorithm applied to clinical ECG mapping data. IEEE Trans Biomed Eng 2002; 49:1153–1164.
20. Ramanathan C, Jia P, Ghanem R, Calvetti D, Rudy Y. Noninvasive electrocardiographic imaging (ECGI): Application of the generalized minimal residual (GMRes) method. Ann Biomed Eng 2003; 31:981–994.
21. Clerc L. Directional differences on impulse spread in trabecular muscle from mammalian heart. J Physiol 1976; 255:335–346.
22. Valderrabano M. Influence of anisotropic conduction properties in the propagation of the cardiac action potential. Prog Biophys Mol Biol 2007; 94:144–168.
23. Helm PA, Younes L, Beg MF, Ennis DB, Leclercq C, Faris OP, McVeigh E, et al. Evidence of structural remodeling in the dyssynchronous failing heart. Circ Res 2006; 98:125–132.
24. Ten Tusscher KHWJ, Panfilov AV. Alternans and spiral breakup in a human ventricular tissue model. Am J Physiol 2006; 291:H1088–H1100.
25. Weber FM, Keller DU, Bauer S, Seemann G, Lorenz C, Dossel O. Predicting tissue conductivity influences on body surface potentials—an efficient approach based on principal component analysis. IEEE Trans Biomed Eng 2011; 58:265–273.
26. Kohl P, Ravens U. Cardiac mechano-electric feedback: Past, present, and prospect. Prog Biophys Mol Biol 2003; 82:3–9.
27. Vetter FJ, McCulloch AD. Mechanoelectric feedback in a model of the passively inflated left ventricle. Ann Biomed Eng 2001; 29:414–426.

28. Jie X, Gurev V, Trayanova N. Mechanisms of mechanically induced spontaneous arrhythmia in acute regional ischemia. Circ Res 2010; 106:185–192.
29. Keller DUJ, Jarrousse O, Fritz T, Ley S, Dossel O, Seemann G. Impact of physiological ventricular deformation on the morphology of the T-wave: A hybrid, static-dynamic approach. IEEE Trans Biomed Eng 2011; 58:2109–2119.
30. Young AA, Frangi AF. Computational cardiac atlases: From patient to population and back. Exp Physiol 2009; 94:578–596.

Supporting Information

Supporting Information may be found in the online version of this article.

Supplementary movie S1. Simultaneous visualization of instantaneous local excitation, depolarization vector, and ECG

Supplementary movie S2. Excitation of the heart and body surface potential of patient #1

Supplementary movie S3. Excitation of the heart and body surface potential of patient #2 without CRT

Supplementary movie S4. Excitation of the heart and body surface potential of patient #2 with CRT

Supplementary movie S5. Excitation of the heart and body surface potential of patient #3 without CRT

Supplementary movie S6. Excitation of the heart and body surface potential of patient #3 with CRT

Supplementary movie S7. Excitation of the heart and body surface potential of patient #4 without CRT

Supplementary movie S8. Excitation of the heart and body surface potential of patient #4 with CRT

Supporting Information may be found in the online version of this article.
(This link will take you to the article abstract.)

Mitochondrial Colocalization with Ca²⁺ Release Sites is Crucial to Cardiac Metabolism

Asuka Hatano,* Jun-ichi Okada, Takumi Washio, Toshiaki Hisada, and Seiryo Sugiura
Department of Frontier Science, The University of Tokyo, Kashiwa, Chiba, Japan

ABSTRACT   In cardiomyocyte subcellular structures, colocalization of mitochondria with Ca²⁺ release sites is implicated in regulation of cardiac energetics by facilitating Ca²⁺ influx into mitochondria to modulate the tricarboxylic acid (TCA) cycle. However, current experimental techniques limit detailed examination of this regulatory mechanism. Earlier, we developed a three-dimensional (3D) finite-element cardiomyocyte model featuring a subcellular structure that integrates excitation-contraction coupling and energy metabolism. Here, using this model, we examined the influence of distance between mitochondria and Ca²⁺ release sites by comparing a normal (50-nm) distance model and a large (200-nm) distance model (LD). The influence of distance was minimal under a low pacing rate (0.25 Hz), but under a higher pacing rate (2 Hz), lower levels of mitochondrial Ca²⁺ and NADH, elevated phosphate, and suppressed force generation became apparent in the LD model. Such differences became greater when functional impairments (reduced TCA cycle activity, uncoupling effect, and failing excitation-contraction coupling) were additionally imposed. We concluded that juxtaposition of the mitochondria and the Ca²⁺ release sites is crucial for rapid signal transmission to maintain cardiac-energy balance. The idealized 3D model of cardiac excitation-contraction and metabolism is a powerful tool to study cardiac energetics.

INTRODUCTION

Recent studies have identified an important role for mitochondrial Ca²⁺ in myocardial energy metabolism by upregulating the tricarboxylic acid (TCA) cycle to stimulate ATP production. Because the rise in cytosolic Ca²⁺ triggers contractions in the sarcomeres—the primary locus of energy consumption—incidental Ca²⁺ flux to mitochondria may constitute a feed-forward regulatory mechanism for rapid and fine tuning of energy balance. However, the high half-maximal effective concentration (EC$_{50}$; ~10 μM) of mitochondrial Ca²⁺ uniporters poses a question as to whether such a mechanism functions in the face of low cytosolic Ca²⁺ transient (peak value, 1–2 μM) (1,2).

Subcellular cardiomyocyte structures may provide a clue to the answer to this question. Electron micrographic studies of subcellular myocyte structures show that mitochondria occupy the entire space between muscle Z-lines; the ends of mitochondria are located near calcium release units (CaRUs), where L-type Ca²⁺ channels (LCCs) and junctional sarcoplasmic reticulum (JSR) face each other in close proximity (3–7). Upon depolarization of the sarcolemma, Ca²⁺ entry through LCCs induces Ca²⁺ release from the JSR and possibly generates a transiently high Ca²⁺ concentration that exceeds the EC$_{50}$ in this subspace, thereby facilitating Ca²⁺ influx to mitochondria (6,8–13). Because of mitochondrial remodeling and dislocation (e.g., swelling, proliferation, and clustering), loss of cytoskeletal connections have been reported in failing myocardium (8,14–16). Elucidation of subcellular structure and function in both healthy and diseased myocardium is of paramount impor-

tance. However, limitations of the available experimental techniques have made it difficult to obtain sufficient information for a thorough understanding of these mechanisms.

We have already developed a three-dimensional (3D) model of cardiomyocytes based on the finite-element method (17–19). In this model, cardiac electrophysiology, contraction, and ATP metabolism localized to specific loci of each organelle, diffusion of Ca²⁺ and energy metabolites, and deformation by sarcomere force generation were simulated in detail with subcellular structures.

In this study, we used this model to study the structure-function relationship of mitochondria in cardiac energy metabolism, with particular focus on the significance of the distance between mitochondria and CaRUs. We found the effect of distance on energetic state to be minimal when myocytes were stimulated at low frequency, but we saw significant differences between the normal and large-distance models in mitochondrial [Ca²⁺], [NADH], and cytosolic phosphate [Pi] at higher stimulation rates. Simulation results of failing myocytes modeling increased proton leak and depressed TCA cycle activity will also be presented.

MATERIALS AND METHODS

3D cardiomyocyte model

The details of 3D cardiomyocyte models have been reported and validated previously (18,19). Briefly, a segment containing three myofibrils of one sarcomere length, together with the adjacent cell membrane and organelle, were modeled by the finite-element method (Fig. 1 A). Subcellular components—including mitochondria, myofibril (A-zone, I-zone, and M-line), JSR, network SR (NSR), surface, and t-tubular sarcolemma—were located at the appropriate finite-element-method nodes to reproduce the anatomical
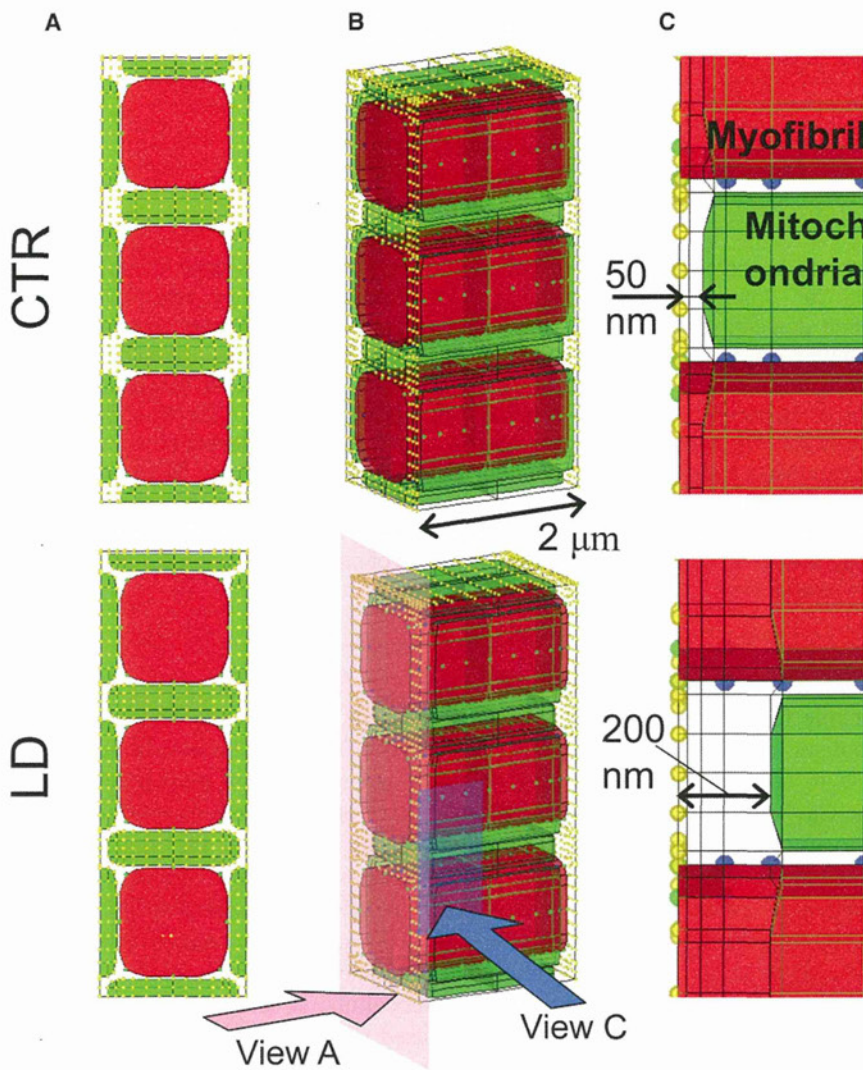
FIGURE 1 Three-dimensional cardiomyocyte models with two different distances between mitochondria and the Ca^{2+} release site: the 50-nm distance model (CTR) (*upper*) and the 200-nm distance model (LD) (*lower*). (*A*) Short-axis views. (*B*) 3D presentations. (*C*) Magnified view of the region near the Ca release sites on the right. Mitochondria are green and myofibrils red. Other subcellular components (channels, pumps, etc.) were assigned to nodes, representing sarcolemma (*yellow*) or SR (*blue*).

structure. Each subcellular component exchanges ions and/or metabolites according to the mathematical formulations expressed as a function of the molecular concentrations in the surrounding cytosol (20,21). These molecules diffuse freely through the cytosolic space; the processes were calculated by solving reaction-diffusion equations. Further details outlining the model can be found in the Supporting Material.

Acto-myosin ATPase model

To examine the influence of metabolic state on the cardiac contraction, we coupled a cross-bridge kinetics model with ATP hydrolysis by myosin (22,23). We adopted a simplified four-state model, schematically shown in Fig. 2 , in which M indicates myosin and A indicates actin. Governing equations are shown in the Appendix, with rate constants taken from the literature (24–27). In this model, [Pi] affects force generation by interfering with the transition from a weakly binding state (A·M·ADP·Pi) to a strongly binding (force-bearing) state (AM·ADP) (28); see also Appendix). Depletion of ATP shifts the distribution into the rigor (AM) state.

The model of Ca^{2+} regulation of contraction was adopted from Rice et al. (29), with parameters refined for guinea pig by Cortassa et al. (20), in which binding of Ca^{2+} to troponin C (TnC) modulates the rate constant of the transition from [A·ATP] to [A·M·ADP·Pi] to cooperatively activate the myofilament. Model equations are shown in the Appendix.

Large-distance model

To investigate the effect of the distance between mitochondria and CaRUs, we created a model with an abnormally large distance (LD) of 200 nm and compared it with a model with a normal-sized 50-nm distance (CTR) (Fig. 1, *A* and *B*). To examine only the effect of the distance between mitochondria and CaRUs, we adjusted the thickness of mitochondria to keep their volume constant in the LD model (Fig. 1 *B*). Accordingly, the volumes of other subcellular structures and the total segment volume were maintained. The normal size, 50 nm, was adopted from electron microscopic observations (8) by taking into account the shrinkage introduced by the fixation procedure (30). The larger size was the maximum value we could attain without changing the volumes of mitochondria, other organelles, and the whole cell.

Failing cardiomyocyte model

Three types of functional abnormality often observed in failing myocardium, i.e., the uncoupling effect (proton leak), depressed TCA cycle activity, and failing excitation-contraction (EC) coupling, were modeled to investigate the influence of distance under diseased conditions. The uncoupling effect was modeled by increasing the proton leak factor, g_H, to 4.0×10^{-5}. The resultant leak flux was comparable to F_0F_1 ATPase
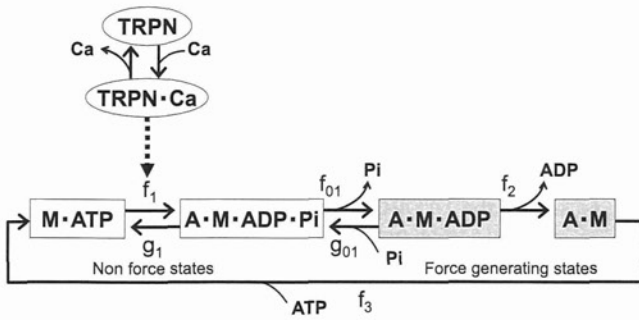
FIGURE 2 State diagrams for the actomyosin ATPase model. A, actin; M, myosin; TRPN, troponin; f_x and g_x, transition rate constants. White boxes correspond to non-force-bearing states. Gray boxes correspond to force-generating states. Transition from M·ATP to A·M·ADP·Pi is cooperatively facilitated by Ca^{2+} binding to troponin. See text for details.

proton flux under pacing at 3 Hz. TCA-cycle activity was depressed by reducing all of the catalytic constants (k_{cat}^{CS}, k_f^{ACO}, k_{cat}^{IDH}, k_{cat}^{KGDH}, k_f^{SL}, k_{cat}^{SDH}, k_f^{FH}, and k_{cat}^{MDH}) by 40%. Failing EC coupling was modeled by decreasing sarcoplasmic Ca^{2+} pump (SERCA) activity (V_{max} 50% of control) and increasing sarcolemmal sodium-calcium exchanger (NCX) activity to 200% of control.

Protocol

Current pulse (100 $\mu A/cm^2$; duration, 0.5 ms) was applied to sarcolemma to simulate electrical pacing. Cardiomyocyte responses to abrupt changes

in workload were examined by switching pacing frequency between 0.25 Hz (low load) and 2 Hz (high load) for comparisons with the experimental study (31).

Calculation

All the program codes were written in-house using Fortran language. Computation was performed using an Intel Xeon CPU (3.2 GHz).

RESULTS

Responses of global and local concentrations of Ca^{2+} and metabolites and ion currents of the CTR model were similar to those reported in our previous article (18).

Effect of distance between mitochondria and Ca^{2+} release site

Fig. 3 (left) compares the responses of mitochondrial $[Ca^{2+}]$ ($[Ca^{2+}]_{mito}$), [NADH], mitochondrial [ADP] ($[ADP]_{mito}$), and cytosolic [Pi] ($[Pi]_{cyto}$) to abrupt changes in pacing rates between CTR (black line) and LD (gray line) models. The responses of the CTR model were similar to our previous results (18) and agree with both previous simulation (20) and experimental (31) studies. The LD model showed a similar pattern of responses under the
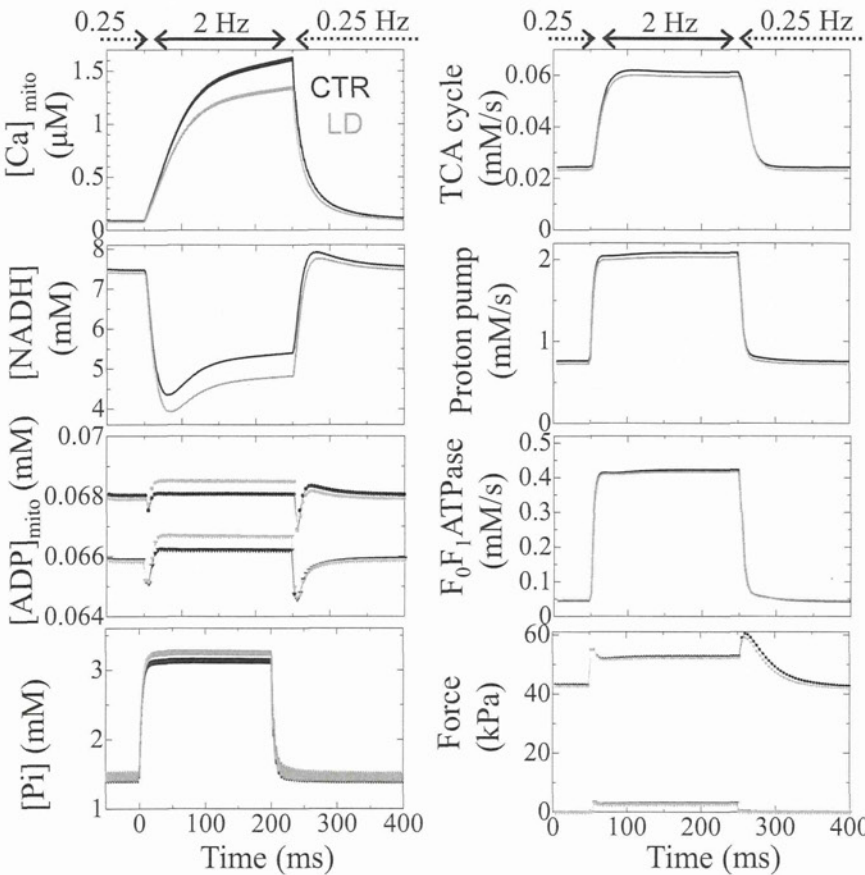

FIGURE 3 Transient responses of the CTR model (black) and the LD model (gray) to abrupt changes in pacing rate between 0.25 Hz and 2 Hz. (Left, top to bottom) Mitochondrial Ca^{2+}, NADH, ADP, and cytosolic Pi concentrations. (Right, top to bottom) Mitochondrial metabolic fluxes for TCA, electron transport chain, and F_0F_1 ATPase, and generated force. In each panel, data averaged over the cytosolic or mitochondrial space are shown. In the graphs of ADP and force, only the maximum (circles) and the minimum (triangles) values are plotted for visibility.

low-workload condition (0.25 Hz), with levels of $[Ca^{2+}]_{mito}$, [NADH], $[ADP]_{mito}$, and [Pi] close to those observed for the CTR model. However, increasing the workload to 2 Hz introduced significant differences in these parameters. After 200 s of 2-Hz pacing, the respective CTR and LD values were 1.63 and 1.35 μM for $[Ca^{2+}]_{mito}$ (−17% relative change); 5.40 and 4.82 mM for [NADH] (−11%); 39.96 and 40.78 μM for $[ADP]_{mito}$ (+2.1%); and 3.16 and 3.28 mM for [Pi] (+3.6%). The developed force dropped 1.1% in LD compared to CTR; thus, ATP consumption by myofibrils decreased in the LD model (data not shown). We also compared fluxes in metabolic pathways between the two models (Fig. 3, *right*) and found that TCA flux (representing NADH production velocity), electron transport chain flux (NADH consumption velocity), and F_0F_1 ATPase flux (ATP production velocity) were all higher in CTR. Values for CTR versus LD at 200 s after the initiation of 2-Hz pacing were 61.2 and 59.5 μM/s for TCA flux (−2.85% relative change), 2.08 and 2.03 mM/s for electron transport chain flux (−2.57%), and 0.422 and 0.417 mM/s for F_0F_1 ATPase flux (−1.35%). We also note that whereas the responses of electron transport chain flux and F_0F_1 ATPase flux were prompt, the response of the TCA cycle was slow, probably reflecting the slow rise and fall in $[Ca^{2+}]_{mito}$.

Spatiotemporal distributions of $[Ca^{2+}]_{cyto}$ and $[ADP]_{cyto}$ are plotted and compared between 0.25 Hz and 2 Hz in Fig. 4 . The black line indicates the position at 50 nm from the Z-line, and the gray line shows the position at

200 nm. Both $[Ca^{2+}]_{cyto}$ and $[ADP]_{cyto}$ display higher concentrations near the Z-line, but the spatial gradient of $[Ca^{2+}]_{cyto}$ is much larger compared to that of $[ADP]_{cyto}$. Rapid pacing at 2 Hz made this gradient steeper, so that the difference in $[Ca^{2+}]_{cyto}$ between 50 nm and 200 nm became greater. On the other hand, although the 2-Hz pacing raised the $[ADP]_{cyto}$ homogeneously, the difference between 50 nm and 200 nm remained small due to the shallow slope in distribution.

Failing-myocyte models

The effect of distance between mitochondria and Ca^{2+} release site on responses to changing workload was examined in the presence of depressed TCA activity (TCA^-; Fig. 5 , *left*), uncoupling effect (UNC; Fig. 5, *middle*), and failing-EC coupling (EC; Fig. 5, *right*). The first two functional abnormalities (TCA^- and UNC) lowered [NADH] at 0.25 Hz (Fig. 5, *rows 2 and 3*), but phosphorylation potential was relatively constant in both CTR and LD models (data not shown). As seen in the absence of functional abnormalities (Fig. 3), rapid pacing at 2 Hz decreased [NADH] and increased $[ADP]_{mito}$ and [Pi], but these changes were greater. Notably, the differences in [Pi] and force at 2 Hz between CTR and LD models also increased with both TCA^- (+9.0%) and UNC (+6.7%) (Fig. 5, *rows 4 and 5*).

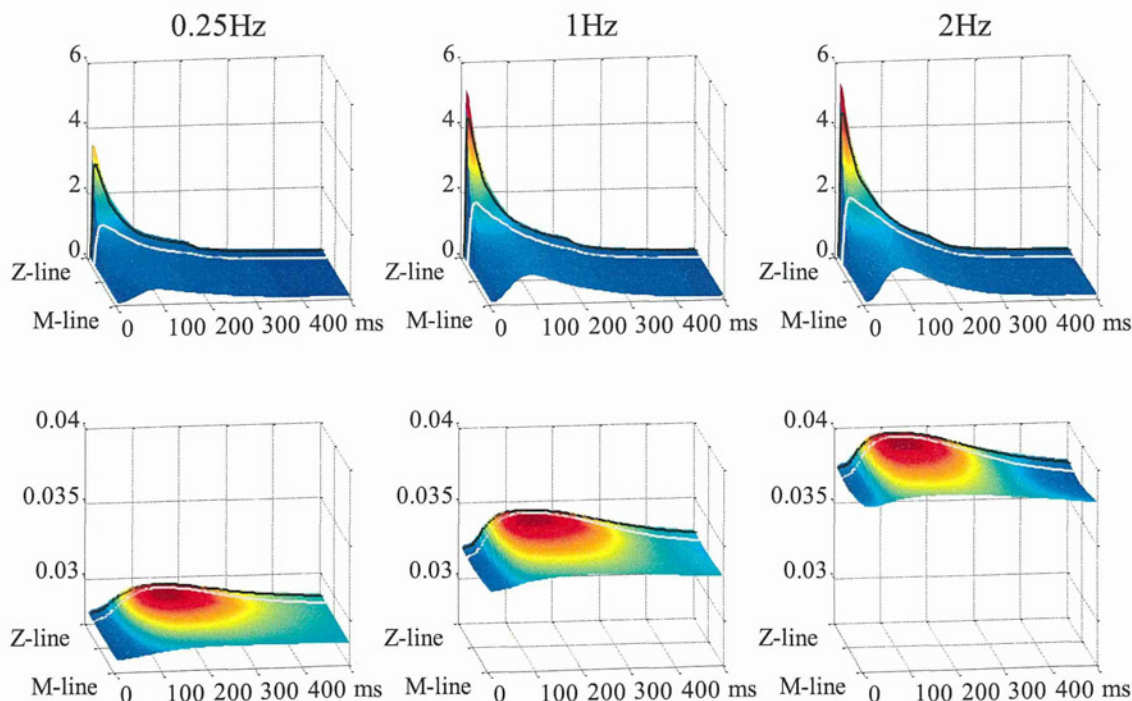However, the two types of functional abnormalities gave distinct response patterns. Although [NADH] dropped

FIGURE 4 Spatiotemporal distributions of cytosolic Ca^{2+} (*upper*) and ADP (*lower*) are shown at pacing rates of 0.25 Hz (*left*), 1 Hz (*middle*), and 2 Hz (*right*). Locations at 50 nm and 200 nm from the Z-line are indicated with black and gray lines, respectively.
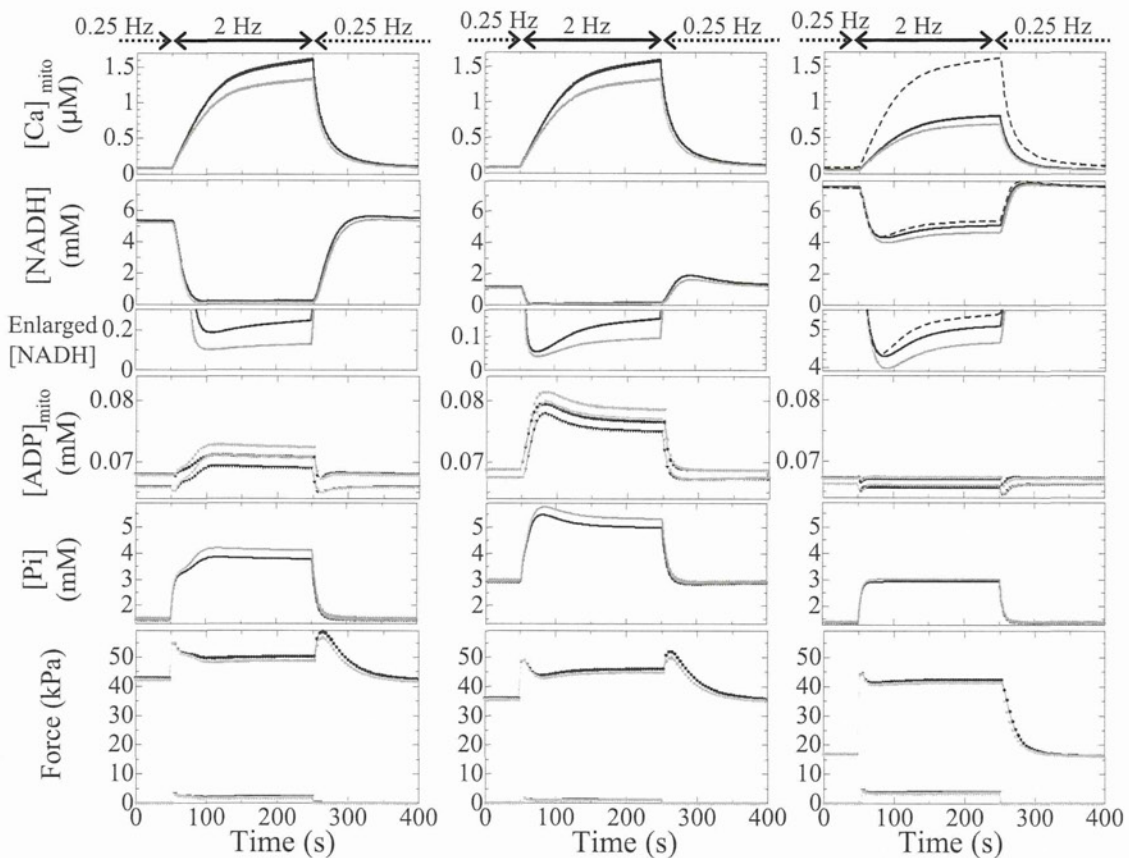
FIGURE 5 Transient responses of the CTR model (*black*) and the LD model (*gray*) under conditions of depressed TCA activity (*left*), uncoupling (*middle*), and failing EC coupling (*right*) with respect to (*top to bottom*) mitochondrial Ca^{2+}, NADH, NADH magnification of bottom parts, mitochondrial ADP, cytosolic Pi, and generated force. Data shown are averaged over the cytosolic or mitochondrial space. In the three upper panels on the right, the responses of the CTR model without functional abnormalities are shown by dashed lines for comparison. In the graphs of ADP and force, only the maximum (*circles*) and minimum (*triangles*) values are plotted for visibility.

acutely upon increasing the pacing rate in both TCA⁻ and UNC models, [ADP] and [Pi] increased gradually only in TCA⁻ models. Moreover, closer examination shows that these gradual increases consisted of a rapid first phase and a slow second phase, with differences between CTR and LD becoming apparent in the second phase. In the UNC model, rapid pacing reduced [NADH] to >0.1 mM within 20 s; [ADP] and [Pi] increased rapidly and monotonically to give even overshoots in both CTR and LD models.

On the other hand, the EC model showed unique responses. Reflecting the decreased Ca^{2+} uptake and release of SR, both force level and mitochondrial Ca^{2+} at 2 Hz were low compared to the control (Fig. 5, *right* (*bottom* and *top*, respectively)), but the reduced energy consumption resulting from the impaired force development made the mitochondrial ADP and Pi responses similar to those of control. The response of NADH to the increased pacing rate showed clear contrast to those of the other two models (Fig. 5, *right*). When the distance between mitochondria and CaRU was small, introduction of the EC condition did not change the initial fall in NADH compared to the

normal-function model (*dashed line*), but the increase in distance significantly decreased it (–7.5%).

DISCUSSION

In this study, we utilized the 3D integrated cardiomyocyte model we developed earlier (18,19) to examine the significance of distance between CaRUs and mitochondria in cardiac energetics. The simulation study gave us a free hand in setting the experimental conditions and allowed us to focus solely on morphological factors that contribute to cardiac energetics.

Subcellular distributions of metabolites

As in our previous studies (18,19), we identified a steep gradient in $[Ca^{2+}]_{cyto}$, ranging from 10 μM near the CaRUs to 0.1 μM in the M-line region. Such a distribution is consistent with experimental findings (32), and could facilitate mitochondrial Ca^{2+} uptake from the Z-line region. ATP and ADP also showed spatial distributions. Contractile myosin activity hydrolyzes ATP, letting ADP accumulate

in the myofibril A-zone. As M-line-bound creatine kinase (CK) synthesizes ATP from ADP, ADP is distributed homogeneously over the myofibril I zone (Fig. 4) and stimulates mitochondrial ATP synthesis (Fig. S1 and Movie S1 in the Supporting Material); ATP and ADP distribution patterns are complementary. Spatial distributions of other metabolites—creatine, creatine phosphate, and Pi—are negligible because of their high diffusiveness.

Effect of distance between mitochondria and Ca^{2+} release site

The effect of distance can be shown by the differences in cytosolic concentration of signal molecules surrounding the mitochondria. Fig. 6 summarizes the regulatory mechanisms of mitochondrial respiration incorporated in this model. Because ATP is synthesized from ADP by F$_0$F$_1$ ATPase, which decreases membrane potential, ATP production is activated in two ways: [Ca^{2+}]$_{mito}$ activates the TCA cycle to produce NADH that is used by the electron transport chain to push up the inner membrane potential (Fig. 6, *red arrows*) and pull up the F$_0$F$_1$ ATPase activity by ADP feedback (Fig. 6, *blue arrow*) (20). Because of the distinct distributions of [Ca^{2+}]$_{cyto}$ and [ADP]$_{cyto}$ described above, CTR myocytes can make full use of both these pushing and pulling effects, whereas the LD myocyte cannot. Rapid pacing increases the Ca^{2+} content of the SR and Ca^{2+} release to raise [Ca^{2+}]$_{mito}$, thereby exaggerating the difference in availability of the pushing-up reactants between the CTR and LD models (Fig. 4). On the other hand, because ADP shows fairly flat distribution along the myofibril, even during rapid pacing, the effect of larger

FIGURE 6 Schematic illustrating the effect of distance between mitochondria and the Ca^{2+} release site. (*Upper*) Positions of mitochondria in the CTR and LD models relative to the typical distributions of [Ca^{2+}]$_{cyto}$ and [ADP]$_{cyto}$. (*Lower*) Summary of the mechanisms regulating mitochondrial metabolism incorporated in our model. Red arrows indicate the pushing-up effect and blue arrows the pulling-up effect on mitochondrial membrane potential to facilitate F$_0$F$_1$ ATPase. See text for details.

distance that emerges under rapid pacing is the pushing-up activation by Ca^{2+}. The decreased pushing-up reactants for the LD model induces lower [NADH] and higher [Pi], resulting in lower force development.

Effect of distance on failing-myocyte models

In diseased myocardium, morphological abnormalities are usually accompanied by functional impairment. Increased levels of mitochondrial uncoupling proteins and decreased mitochondrial efficiency have been reported in heart failure (33). Decreased TCA cycle flux without anaplerosis might also be responsible for the contractile failure (34,35). Both depressed TCA cycle activity and uncoupling decrease the baseline (0.25 Hz) [NADH] level and expand differences in [ADP]$_{mito}$, [Pi]$_{cyto}$, and force between CTR and LD models under high workload. The reason for this enhanced difference is the higher gain of electron transport chain activity to [NADH] when it is <0.5 mM (Fig. 5, *row 3*) (36). Although the depression in force in these failing-myocyte models is still relatively small, its effect in combination with other abnormalities may cause severe disorders in cardiac function.

This response pattern may provide an insight into the mechanism. Depression of the TCA cycle significantly retarded the response to the abrupt change in workload (Fig. 5). Because the TCA cycle plays a central role in the pushing-up mechanism (Fig. 6), the loss of this feedforward mechanism is expected to slow response, whereas the proton leak reduces the efficiency of ATP synthesis; thus, greater ADP feedback signals are required to meet the higher workload.

We also examined the responses of the failing-EC-coupling model characterized by reduced energy consumption (impaired force generation) and normal mitochondrial function. The initial fall of NADH in response to increased pacing rate was much larger than those of two other disease models but comparable to the normal model. The normally functioning respiratory chain in this model responded even to a small ADP signal to cause the initial fall in NADH (owing to its conversion to NAD$^+$ for ATP production), but the Ca^{2+}-sensitive pushing-up mechanism (NADH production via the TCA cycle) counteracts this initial fall, depending on the distance between mitochondria and the Ca release site.

Taken together, this simulation study indicated that the effect of the distance between mitochondria and the Ca release site significantly affects regulation of NADH dynamics in response to abrupt change in pacing rate only when both TCA cycle and respiratory chain in mitochondria function normally; the function of EC coupling proteins may not be a dominant factor.

Very recently, Chen et al. (37) studied the role of Mitofusion 2 (Mfn2) protein, which tethers the mitochondria and SR, and found a large initial drop in NADH with
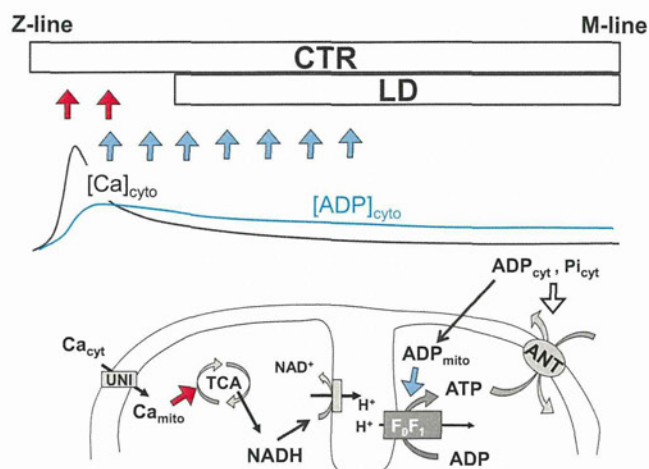
rapid pacing in Mfn2-deficient myocytes compared to the wild-type. Because they did not detect any significant changes in expression and function of EC coupling proteins, despite prominent alterations in mitochondrial SR architecture, they concluded that the physical tethering of SR and mitochondria via Mfn2 is essential for cardiomyocyte bioenergetics feedback response. These experimental results are consistent with those of the simulation study presented here, thus validating our 3D myocyte model.

Study limitation

In this study, due to the limitation in computational power, we had to use a small-scale model that assumed periodicity and symmetry. Therefore, we focused on the effect of distances between mitochondria and CaRUs by changing them uniformly along the t-tubule. Because the configuration of the resultant model was physiologically unrealistic, we performed a simulation on a model in which the distances were periodically different (Fig. A2 A in the Appendix). As shown in (Fig. A2 B, see figure in the Appendix), however, we could obtain an intermediate result between the control and the uniform large-distance models. A future study using a larger-scale model is necessary to examine the effect of heterogeneous distribution of distances between mitochondria and CaRUs.

CONCLUSION

Our 3D model showed that the small difference in distance between CaRUs and mitochondria could alter metabolic control, reduce robustness to change in workload, and make the cell vulnerable to several pathological conditions. We suggest that juxtaposition of the mitochondria to CaRU is crucial for rapid signal transmission to maintain cardiac energy balance. The 3D integrated model of cardiac EC and metabolism provides a powerful tool for investigating cardiomyocyte physiology in ways not afforded by other experimental methods.

APPENDIX

Equations describing the sarcomere dynamics:

$$\frac{d[A \cdot M \cdot ADP \cdot Pi]}{dt} = -(g_1 + f_{01})[A \cdot M \cdot ADP \cdot Pi] + g_{01}[Pi][A \cdot M \cdot ADP] + f_1[M \cdot ATP] \tag{A1}$$

$$\frac{d[A \cdot M \cdot ADP]}{dt} = -f_2[A \cdot M \cdot ADP] - g_{01}[Pi][A \cdot M \cdot ADP] + f_{01}[A \cdot M \cdot ADP \cdot Pi] \tag{A2}$$

$$\frac{d[A \cdot M]}{dt} = -f_3[A \cdot M] - f_2[A \cdot M \cdot ADP] \tag{A3}$$

$$\frac{d[M \cdot ATP]}{dt} = -f_1[M \cdot ATP] + f_3[A \cdot M] + g_1[A \cdot M \cdot ADP \cdot Pi] \tag{A4}$$

$$\frac{d[LTRPN \cdot Ca]}{dt} = k_p^{ltrpn}([LTRPN]_{tot} - [LTRPN \cdot Ca]) - k_m^{ltrpn}[LTRPN][Ca] \tag{A5}$$

$$f_1 = f_1^{max}[LTRPN \cdot Ca]^5 \tag{A6}$$

$$f_3 = f_3^{max}\left\{ \left(1 + \frac{K_m}{[ATP]}\right)\left(1 + \frac{[ADP]}{K_i}\right) \right\}^{-1} \tag{A7}$$

TABLE A1 Parameter values of acto-myosin ATPase model

Parameter	Value	Unit	Description	Reference
f_{01}	1.2	ms^{-1}	Rate constant from $A \cdot M \cdot ADP \cdot Pi$ to $A \cdot M \cdot ADP$	(27) [a]
g_{01}^{min}	0.08	$mM^{-1} ms^{-1}$	Minimum rate constant from $A \cdot M \cdot ADP$ to $A \cdot M \cdot ADP \cdot Pi$	(27) [a]
f_1^{max}	0.005	ms^{-1}	Maximum rate constant from $M \cdot ATP$ to $A \cdot M \cdot ADP \cdot Pi$	
g_1	0.05	ms^{-1}	Rate constant from $A \cdot M \cdot ADP \cdot Pi$ to $M \cdot ATP$	
f_2	0.004	ms^{-1}	Rate constant from $A \cdot M \cdot ADP$ to $A \cdot M$	
f_3^{max}	0.9	ms^{-1}	Maximum rate constant for $A \cdot M$ to $M \cdot ATP$	
K_m	0.03	mM	ATP half-saturation constant	(25)
K_i	0.1	mM	ADP inhibition constant	(26)
k_p^{ltrpn}	100	ms^{-1}	Ca^{2+} on-rate for troponin low-affinity sites	(20)
k_m^{ltrpn}	4.0×10^{-2}	$mM^{-1} ms^{-1}$	Ca^{2+} off-rate for troponin low-affinity sites	(20)
$[LTRPN]_{tot}$	0.07	mM	Total troponin low-affinity sites	
ζ	0.1	$mM^{-1} kPa$	Conversion factor normalizing to physiological force	

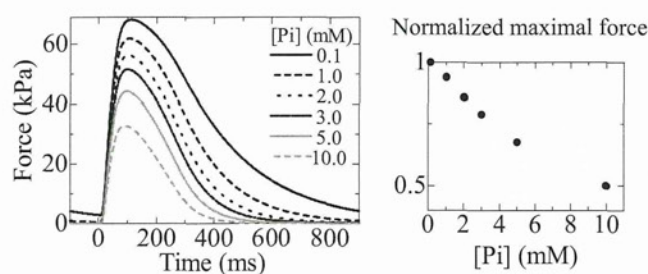[a]Parameters were doubled considering the temperature.

FIGURE A1 (*Left*) Time courses of twitch force under various [Pi] (0.1, 1.0, 2.0, 3.0, 5.0, and 10.0 mM). (*Right*) Normalized maximal twitch force as a function of [Pi].

$$g_{01} = g_{01}^{min}\left(1 + \frac{2.3 - SL}{(2.3 - 1.7)^{1.6}}\right) \quad \text{(A8)}$$

$$Force = \zeta([A \cdot M \cdot ADP] + [A \cdot M]) \quad \text{(A9)}$$

$$V_{AM} = f_3[A \cdot M] \quad \text{(A10)}$$

A, actin; LTRPN, troponin low-affinity sites; M, myosin; SL, sarcomere length; V_{AM}, ATPase rate. Parameters are shown in Table A1 .

Fig. A1 , *left*, shows the isometric twitch force of the CTR model paced at 1 Hz under various [Pi] conditions. Peak twitch force decreases almost linearly with increasing [Pi], and at 10 mM [Pi], the peak twitch force becomes about half of that under 0.1 mM [Pi] (Fig. A2, *right*).

SUPPORTING MATERIAL

Supplemental methods, one figure, and two movies are available at http://www.biophysj.org/biophysj/supplemental/S0006-3495(12)05113-2.

REFERENCES

1. Gunter, T. E., K. K. Gunter, ..., C. E. Gavin. 1994. Mitochondrial calcium transport: physiological and pathological relevance. *Am. J. Physiol.* 267:C313–C339.

2. Sedova, M., E. N. Dedkova, and L. A. Blatter. 2006. Integration of rapid cytosolic Ca^{2+} signals by mitochondria in cat ventricular myocytes. *Am. J. Physiol. Cell Physiol.* 291:C840–C850.

3. Fawcett, D. W., and N. S. McNutt. 1969. The ultrastructure of the cat myocardium. I. Ventricular papillary muscle. *J. Cell Biol.* 42:1–45.

4. Ohata, H., E. Chacon, ..., J. J. Lemasters. 1998. Mitochondrial Ca^{2+} transients in cardiac myocytes during the excitation-contraction cycle: effects of pacing and hormonal stimulation. *J. Bioenerg. Biomembr.* 30:207–222.

5. Csordás, G., A. P. Thomas, and G. Hajnóczky. 2001. Calcium signal transmission between ryanodine receptors and mitochondria in cardiac muscle. *Trends Cardiovasc. Med.* 11:269–275.

6. Lukyanenko, V., A. Chikando, and W. J. Lederer. 2009. Mitochondria in cardiomyocyte Ca^{2+} signaling. *Int. J. Biochem. Cell Biol.* 41:1957–1971.

7. Hayashi, T., M. E. Martone, ..., M. Hoshijima. 2009. Three-dimensional electron microscopy reveals new details of membrane systems for Ca^{2+} signaling in the heart. *J. Cell Sci.* 122:1005–1013.

8. Sharma, V. K., V. Ramesh, ..., S. S. Sheu. 2000. Transport of Ca^{2+} from sarcoplasmic reticulum to mitochondria in rat ventricular myocytes. *J. Bioenerg. Biomembr.* 32:97–104.

9. Bers, D. M. 2002. Cardiac excitation-contraction coupling. *Nature.* 415:198–205.

10. Shannon, T. R., F. Wang, ..., D. M. Bers. 2004. A mathematical treatment of integrated Ca dynamics within the ventricular myocyte. *Biophys. J.* 87:3351–3371.

11. Maack, C., S. Cortassa, ..., B. O'Rourke. 2006. Elevated cytosolic Na$^+$ decreases mitochondrial Ca^{2+} uptake during excitation-contraction coupling and impairs energetic adaptation in cardiac myocytes. *Circ. Res.* 99:172–182.

12. Belmonte, S., and M. Morad. 2008. "Pressure-flow"-triggered intracellular Ca^{2+} transients in rat cardiac myocytes: possible mechanisms and role of mitochondria. *J. Physiol.* 586:1379–1397.

13. O'Rourke, B., and L. A. Blatter. 2009. Mitochondrial Ca^{2+} uptake: tortoise or hare? *J. Mol. Cell. Cardiol.* 46:767–774.
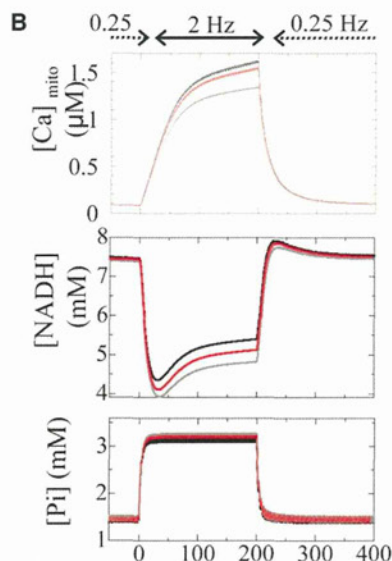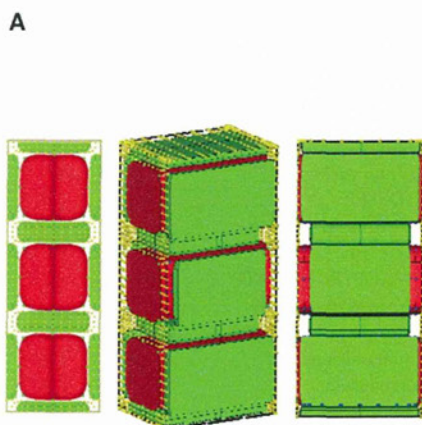

FIGURE A2 (*A*) Model with mixed distances between mitochondria and CaRUs. The distances were adjusted to 50, 200, and 50 nm. (*B*) Reponses of [Ca]$_{mito}$ (*upper*), NADH (*middle*), and Pi (*lower*) to alterations in pacing rate. Black line, control model (distance = 50 nm); gray line, large-distance model (distance = 200 nm); red line, mixed distance.

14. Milner, D. J., M. Mavroidis, ..., Y. Capetanaki. 2000. Desmin cytoskeleton linked to muscle mitochondrial distribution and respiratory function. *J. Cell Biol.* 150:1283–1298.

15. Capetanaki, Y. 2002. Desmin cytoskeleton: a potential regulator of muscle mitochondrial behavior and function. *Trends Cardiovasc. Med.* 12:339–348.

16. Maloyan, A., A. Sanbe, ..., J. Robbins. 2005. Mitochondrial dysfunction and apoptosis underlie the pathogenic process in α-B-crystallin desmin-related cardiomyopathy. *Circulation.* 112:3451–3461.

17. Hatano, A., J. Okada, ..., S. Sugiura. 2011. Juxtaposition of mitochondria to the Ca^{2+} release site is crucial for the cardiac energy balance: a 3-D simulation study of cardiomyocyte. *Trans. Jap. Soc. Med. Biolog. Eng.* 49:829–835.

18. Hatano, A., J. Okada, ..., S. Sugiura. 2011. A three-dimensional simulation model of cardiomyocyte integrating excitation-contraction coupling and metabolism. *Biophys. J.* 101:2601–2610.

19. Hatano, A., J. Okada, ..., S. Sugiura. 2012. Critical role of cardiac t-tubule system for the maintenance of contractile function revealed by a 3D integrated model of cardiomyocytes. *J. Biomech.* 45:815–823.

20. Cortassa, S., M. A. Aon, ..., R. L. Winslow. 2006. A computational model integrating electrophysiology, contraction, and mitochondrial bioenergetics in the ventricular myocyte. *Biophys. J.* 91:1564–1589.

21. Dash, R. K., and D. A. Beard. 2008. Analysis of cardiac mitochondrial Na^+-Ca^{2+} exchanger kinetics with a biophysical model of mitochondrial Ca^{2+} handling suggests a 3:1 stoichiometry. *J. Physiol.* 586:3267–3285.

22. Hibberd, M. G., J. A. Dantzig, ..., Y. E. Goldman. 1985. Phosphate release and force generation in skeletal muscle fibers. *Science.* 228:1317–1319.

23. Goldman, Y. E., and B. Brenner. 1987. Special topic: molecular mechanism of muscle contraction. General introduction. *Annu. Rev. Physiol.* 49:629–636.

24. Kawai, M., Y. Saeki, and Y. Zhao. 1993. Crossbridge scheme and the kinetic constants of elementary steps deduced from chemically skinned papillary and trabeculae muscles of the ferret. *Circ. Res.* 73:33–50.

25. Sugiura, S., H. Yamashita, ..., T. Sugimoto. 1992. Active movement of cardiac myosin on *Characeae* actin cables. *Pflugers Arch.* 421:32–36.

26. Yamashita, H., M. Sata, ..., M. Iizuka. 1994. ADP inhibits the sliding velocity of fluorescent actin filaments on cardiac and skeletal myosins. *Circ. Res.* 74:1027–1033.

27. Araujo, A., and J. W. Walker. 1996. Phosphate release and force generation in cardiac myocytes investigated with caged phosphate and caged calcium. *Biophys. J.* 70:2316–2326.

28. Kusuoka, H., M. Inoue, ..., H. Watari. 1986. Cyclical changes in energy-related metabolites in myocardium detected by phosphorus nuclear magnetic resonance. *In* New Approaches in Cardiac Mechanics. A. H. Kitamura, H. Abe, and K. Sagawa, editors. Routledge, Tokyo. 99–109.

29. Rice, J. J., R. L. Winslow, and W. C. Hunter. 1999. Comparison of putative cooperative mechanisms in cardiac muscle: length dependence and dynamic responses. *Am. J. Physiol.* 276:H1734–H1754.

30. Parfenov, A. S., V. Salnikov, ..., V. Lukyánenko. 2006. Aqueous diffusion pathways as a part of the ventricular cell ultrastructure. *Biophys. J.* 90:1107–1119.

31. Brandes, R., and D. M. Bers. 2002. Simultaneous measurements of mitochondrial NADH and Ca^{2+} during increased work in intact rat heart trabeculae. *Biophys. J.* 83:587–604.

32. Weber, C. R., V. Piacentino, 3rd, ..., D. M. Bers. 2002. Na^+-Ca^{2+} exchange current and submembrane $[Ca^{2+}]$ during the cardiac action potential. *Circ. Res.* 90:182–189.

33. Abel, E. D., and T. Doenst. 2011. Mitochondrial adaptations to physiological vs. pathological cardiac hypertrophy. *Cardiovasc. Res.* 90:234–242.

34. Russell, 3rd, R. R., and H. Taegtmeyer. 1991. Changes in citric acid cycle flux and anaplerosis antedate the functional decline in isolated rat hearts utilizing acetoacetate. *J. Clin. Invest.* 87:384–390.

35. Gibala, M. J., M. E. Young, and H. Taegtmeyer. 2000. Anaplerosis of the citric acid cycle: role in energy metabolism of heart and skeletal muscle. *Acta Physiol. Scand.* 168:657–665.

36. Magnus, G., and J. Keizer. 1997. Minimal model of β-cell mitochondrial Ca^{2+} handling. *Am. J. Physiol.* 273:C717–C733.

37. Chen, Y., G. Csordás, ..., C. Maack. 2012. Mitofusin 2-containing mitochondrial-reticular microdomains direct rapid cardiomyocyte bioenergetic responses via interorganelle Ca^{2+} crosstalk. *Circ. Res.* 111:863–875.

International Heart Journal